



Published in final edited form as:

J Am Chem Soc. 2021 February 10; 143(5): 2304–2314. doi:10.1021/jacs.0c11382.

Voltage imaging with a NIR-absorbing phosphine oxide rhodamine voltage reporter

Monica A. Gonzalez^{*,†}, Alison S. Walker^{*,†}, Kevin J. Cao[§], Julia R. Lazzari-Dean[‡], Nicholas S. Settineri[‡], Eui Ju Kong[‡], Richard H. Kramer^{§,†}, Evan W. Miller^{‡,§,†,*}

[‡]Department of Chemistry, University of California, Berkeley, California 94720, United States.

[§]Department of Molecular & Cell Biology, University of California, Berkeley, California 94720, United States.

[†]Department of Helen Wills Neuroscience Institute. University of California, Berkeley, California 94720, United States.

Abstract

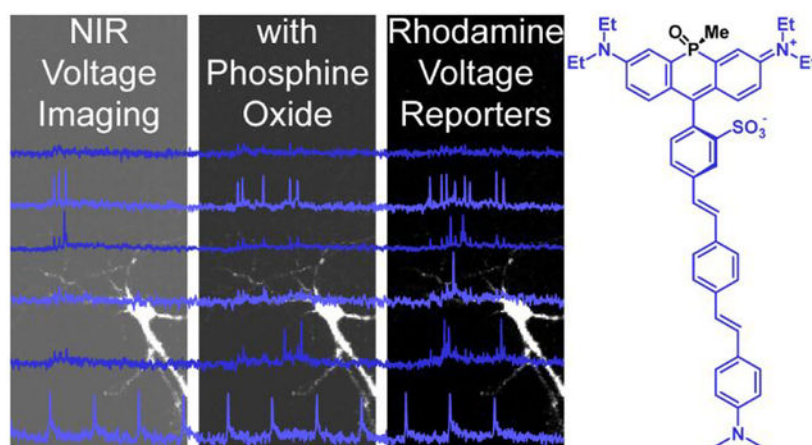
Developing fluorescent dyes that emit and absorb light at wavelengths greater than 700 nm and that respond to biochemical and biophysical events in living systems remains an outstanding challenge for non-invasive optical imaging. Here, we report the design, synthesis, and application of near infrared (NIR)-absorbing and -emitting optical voltmeter based on a sulfonated, phosphine-oxide (po) rhodamine for voltage imaging in intact retinas. We find po-rhodamine based voltage reporters, or poRhoVRs, display NIR excitation and emission profiles at greater than 700 nm, show a range of voltage sensitivities (13 to 43% F/F per 100 mV in HEK cells), and can be combined with existing optical sensors, like Ca²⁺-sensitive fluorescent proteins (GCaMP), and actuators, like light-activated opsins ChannelRhodopsin-2 (ChR2). Simultaneous voltage and Ca²⁺ imaging reveals differences in activity dynamics in rat hippocampal neurons, and pairing poRhoVR with blue-light based ChR2 affords all-optical electrophysiology. In *ex vivo* retinas isolated from a mouse model of retinal degeneration, poRhoVR, together with GCaMP-based Ca²⁺ imaging and traditional multi-electrode array (MEA) recording, can provide a comprehensive physiological activity profile of neuronal activity, revealing differences in voltage and Ca²⁺ dynamics within hyperactive networks of the mouse retina. Taken together, these experiments establish that poRhoVR will open new horizons in optical interrogation of cellular and neuronal physiology in intact systems.

Graphical Abstract

[†]Corresponding Author: evanwmiller@berkeley.edu.

^{**}These authors contributed equally.

Supplementary data, including supporting figures, spectra, procedures, and analysis. This material is available free of charge via the Internet at <http://pubs.acs.org>.



INTRODUCTION

Fluorescence microscopy has revolutionized the life sciences. Advances in both synthetic and genetically encoded fluorophores make fluorescence microscopy routine in laboratories across the globe. Coupled with progress in areas like super-resolution microscopy,¹ light sheet microscopy,² and tissue clearing,^{3–5} fluorescent dyes bring the high spatial and temporal resolution of optical microscopy to bear on samples ranging from single molecules to interacting cells.

However, non-invasive optical imaging in intact tissues and organisms remains challenging. Commonly used fluorophores, like fluorescein and rhodamine, possess excitation and emission profiles within the visible region of the spectrum and overlap extensively with endogenous chromophores, especially heme.^{6–7} Although alternative imaging modalities like magnetic resonance imaging, positron emission tomography, and photoacoustic imaging afford excellent penetration into thick tissue, these modalities require specialized instrumentation, are half-life limited, require radioactive reagents, and/or cannot access the micrometer spatial and millisecond time resolution routinely afforded by optical microscopy.⁸

In the context of neurobiology, an outstanding challenge is tracking neuronal voltage dynamics with sub-micron spatial resolution and sub-millisecond temporal resolution within intact tissues. Although two-photon (2P) microscopy provides access to structures in deeper tissue, traditional raster-scanning 2P microscopy cannot achieve the temporal resolution required to image large numbers of neurons simultaneously.⁹

Therefore, fluorescent dyes and voltage indicators that possess near-infrared (NIR, 700 – 1000 nm)^{10–14} excitation and emission profiles are of considerable interest. First, NIR photons scatter less than visible photons in thick tissue. Second, by avoiding endogenous chromophores like heme (<650 nm) and water (>900 nm),^{6–7, 15} fluorophores that operate in the so-called NIR window gain profound advantages for tissue and *in vivo* imaging. Finally, NIR fluorophores can be more readily deployed for multiplex imaging alongside existing

fluorescent labels, indicators, and actuators that use visible wavelengths of light, on account of the larger spectral separation between the two.

Despite the attraction of NIR dyes that both absorb and emit at wavelengths above 700 nm, traditionally-employed NIR dyes, such as porphyrins and phthalocyanins,¹⁰ polymethines,¹⁰ BODIPY derivatives,^{16–18} and xanthenes with extended annulation^{19–21} tend to suffer from high molecular weights, low water solubility, a propensity to aggregate, and chemical or photochemical instability, complicating their use in biological contexts. A number of creative approaches have recently been employed to address these concerns.^{14, 20, 22–24} In particular, the compact, fused 3-ring system of xanthene-based dyes promotes stability and decreases molecular weight. Annulation of xanthenes can push their absorbance above 700 nm,¹⁹ but at the expense of decreased water solubility. Recent efforts replace oxygen at position 10 with carbon^{25–27} or heteroatoms such as Si,^{28–30} S,³¹ and P. Indeed, recent examples of phosphinate³² and phosphine-oxide based xanthene dyes^{33–34} demonstrate this unique scaffold can access absorption profiles at or above 700 nm while maintaining a compact, three-ring structure.

While numerous approaches to NIR-*emitting* fluorophores exist, there are relatively few examples of NIR-*absorbing* fluorescent *reporters*—fluorophores that sense and respond reversibly to changes in a specific physiological phenomena, for example, metal ions, reactive oxygen species, or transmembrane potential. The few examples of NIR-absorbing indicators employ polymethine, rather than xanthene, scaffolds.^{4, 35–37} Therefore, we were eager to adapt phosphorous-substituted xanthenes into a fluorescent voltage-sensing scaffold. Previous work in our lab suggests that xanthene dyes with a range of bridgehead (O,³⁸ C,²⁷ Si³⁹) and terminal atoms (O^{27, 38} or substituted N^{39–40}) can be employed as voltage-sensitive dyes via introduction of a lipophilic, conjugated molecular wire. We hypothesized that the installation of phenylene vinylene molecular wires into the context of a phosphorous-substituted xanthene dye would yield voltage-sensitive indicators with peak excitation above 700 nm. There are no examples of xanthene-based voltage-sensitive fluorophores with peak excitation above 700 nm, although there are a few examples of chemically-synthesized^{41–44} and genetically encoded^{45–47} voltage indicators with emission maxima beyond 700 nm.

We now present the phosphine-oxide **Rhodamine Voltage Reporters**, or poRhoVRs, which all feature excitation and emission maxima above 700 nm, 13% to 43% F/F per 100 mV voltage sensitivity, and compatibility with commonly used optical sensors and actuators, including Oregon Green BAPTA (OGB), GCaMP6, and ChannelRhodopsin-2 (ChR2). We use poRhoVR to provide the first direct voltage imaging of neuronal hyperactivity in retinas isolated from a mouse model of retinopathy.

Results

Synthesis of sulfonated phosphorous rhodamines

Although phosphorous rhodamines possess attractive optical properties^{32–34} – NIR excitation and emission, photostability,^{32–34} and good water solubility – their tendency to localize to intracellular membranes, including mitochondria³⁴ and lysosomes,⁴⁸ precludes

their straightforward deployment as cytosolic indicators or voltage sensors. Water solubility and exclusion from cellular uptake can be achieved through installation of anionic groups on the exocyclic rhodamine nitrogens;^{49–50} however, we recently found that sulfonation of the *meso* aromatic ring of rhodamine-type systems prevents cellular uptake of dyes.^{39, 51} We hypothesized that a similar strategy could provide sulfonated phosphorous rhodamines for incorporation into voltage sensing scaffolds.

Phosphine-oxide RhoVRs were accessed in 6 steps from commercially available triphenylphosphonium salts (Scheme S1). Anilino phosphine oxide **4** was prepared in high yield over three steps.^{33, 52} Phosphine oxide **4** was alkylated through a slightly modified procedure using ethyl iodide and potassium carbonate in dimethylformamide (DMF) to produce phosphine oxide **5** in 89% yield. The key sulfonated phosphorous rhodamine precursors with bromine substitution for installation of the phenylene vinylene molecular wire were prepared in one step by condensing bromosulfo-benzaldehydes⁵¹ **6** or **7** with phosphine oxide **5** in the presence of urea⁵³ and glacial acetic acid (Scheme 1). Traditional methods for acid-catalyzed construction of rhodamines or sulfonrhodamines, for example, condensation with methane sulfonic acid⁵⁴ or propionic acid without urea^{40, 55} resulted in no reaction or were extremely low yielding.

The condensation between *m*- (**6**) or *p*- bromosulfo-benzaldehyde (**7**) and phosphine oxide **5** produced two isomers of *m*- (**8**) and *p*- (**9**) bromosulfo-phosphine oxide rhodamines^{33–34} in which the P-methyl substituent and sulfonate exist in either a *cis* or *trans* relationship to one another (Figure 1b), consistent with previous reports and nomenclature³³ (Figure S1). For both **8** and **9**, the two isomers were separable on a basic alumina column, eluting with 0–5% methanol in dichloromethane. After this step, no further purification was necessary for the major isomer of either **8** or **9**. Preparative HPLC was required to isolate the minor isomer. Analysis of the NMR spectra of the purified major and minor isomers of **8** and **9** revealed differences in the chemical shifts of both the phosphorous atom and the P-methyl substituents (Table S1): for the P-methyl group, $\delta = 2.00$ ppm (¹H, major isomer) and $\delta = 1.96$ (and Figure S1). Furthermore, x-ray crystal structures of the major isomer of both **8** and **9** reveal a *cis* relationship between the sulfonate and the methyl group on the phosphorous bridgehead atom (Figure 1c and d). Attempts to crystalize the minor isomer of **8** or **9** were unfruitful. In aqueous solution (phosphate buffered saline, 5 μ M dye), both bromo phosphine oxide rhodamine **8** – *cis* and **9** – *cis* had an absorption maximum at 704 nm, emission maxima around 728 nm (Figure 1a), and quantum yields near 20% (22% for **8** and 19% for **9**).

Synthesis of phosphorous rhodamine voltage reporters

After determining that sulfonated po-rhodamines have reasonable quantum yields and desirable NIR excitation and emission maxima above 700 nm, we hypothesized that incorporation of phenylene vinylene molecular wires should render these NIR xanthenes voltage-sensitive. We installed molecular wires **10** (dimethyl aniline) or **11** (diethyl aniline and methoxy substituent) onto the phosphine-oxide rhodamine fluorophore using a Pd-catalyzed Heck coupling to generate a total of four new phosphine oxide Rhodamine VoltageReporters (poRhoVRs, **12** – **15**, Scheme 1). For each reaction, the cross coupling

was performed using the purified, major isomer (*cis*) of either **8** or **9**. However, in each case this did not prevent the formation of *cis/trans* isomers in the complete poRhoVR molecules: analytical HPLC/MS showed two peaks with the product mass corresponding to poRhoVR. As previously reported,³³ separation of the isomers is extremely arduous but in the case of **13**, extensive column chromatography on silica gel and preparative scale HPLC on C₁₈-functionalized silica afforded small quantities of major (9 % yield) and even smaller quantities of minor isomers (1% yield). Comparison of the ¹H and ³¹P NMR data for the isomers of **13** closely match the chemical shifts observed for the *cis* and *trans* isomers of **8** and **9**, suggesting that the major product is the *cis* isomer of **13** (Figure S1). Isomers of the other three poRhoVRs (**12**, **14**, and **15**) were not separated due to the difficulty of purification. ³¹P showed that for poRhoVRs **12**, **14** and **15** major products isolated were *cis* (³¹P δ = 20 ppm), consistent with the results for poRhoVR **13** – *cis* (³¹P δ = 20.2 ppm).

All of the poRhoVR compounds possess excitation and emission profiles well-matched to the parent phosphine-oxide rhodamines: absorption was maximal at 700 nm, and emission peaked at around 728 nm (Table 1, Figure S3a–d).

Cellular characterization of phosphorous rhodamine voltage reporters

All four poRhoVR dyes (**12** – **15**) localize to the cellular membrane and display differing cellular brightness when applied to HEK cells under identical experimental conditions (Figure S2a–d). Although all poRhoVRs localize to the membrane, poRhoVRs **13** and **15**, with N,N-diethyl, methoxyaniline substituents, are approximately 10-fold dimmer in cell membranes than poRhoVR **12** and **14** (N,N-dimethyl aniline) (Table 1, Figure S2e). The long wavelength excitation and emission of poRhoVRs enables multi-color imaging with organelle specific dyes. Live-cell imaging⁵⁶ of poRhoVR **14** (1 μM, Figure 2a) in HEK cells co-stained with rhodamine 123⁵⁷ (the methyl ester of rhodamine 110),⁵⁸ which localizes to the mitochondria on account of its overall positive charge (Figure 2b) and Hoechst 33342,⁵⁹ a bisbenzimidazole dye which binds to nucleic acid, labeling the nuclei of cells, (Figure 2c) demonstrate good membrane localization for poRhoVRs along with compatibility with simultaneous, multi-color imaging (Figure 2d).

The cellular fluorescence of poRhoVRs is voltage sensitive. Simultaneous fluorescence microscopy during sequential depolarizing and hyperpolarizing steps from a holding potential of –60 mV in HEK cells under whole-cell voltage-clamp conditions reveals linear fluorescence vs. voltage relationships for poRhoVR dyes **12** – **14** (Figure 2e and f, **14**; Figure S3 for all indicators). Voltage sensitivities range from 13% (poRhoVR **12**) to 43% (poRhoVR **13**) per 100 mV (Table 1). The sensitivity of poRhoVR **13**, at 43%, is nearly 2-fold the sensitivity of our most red-shifted voltage indicator to date, the Si-rhodamine based BeRST (24% F/F per 100 mV)³⁹ and is comparable to the sensitivity of our previously reported, tetramethyl rhodamine based RhoVR (47% F/F per 100 mV).⁴⁰ However, the low cellular brightness of poRhoVR **13** (more than 10x dimmer than poRhoVRs **12** and **14**) means that indicators like poRhoVR **14**, with intermediate voltage sensitivity (17% F/F per 100 mV), but high cellular brightness (12x brighter, compared to **13**) are also attractive for monitoring voltage dynamics in living systems. This is because, in a shot-noise-limited system, SNR scales with the square root of the number of collected photons, or the cellular

brightness.^{60–61} Therefore, even indicators with only middling F/F values can be quite effective detectors of rapid voltage changes.^{62–63} For poRhoVR indicators, it appears that the OMe-substituted compounds (**13** and **15**) show lower cellular brightness compared to the unsubstituted aniline molecular wires of **12** and **14** (Table 1). This effect appears to be specific to poRhoVR indicators, as rhodamine-based RhoVR indicators show the highest SNR values for OMe-substituted molecular wires.⁴⁰

We evaluated both poRhoVR **13** and **14** in cultured hippocampal neurons isolated from rat embryos. We selected **13** and **14** to investigate whether a bright, but less sensitive dye (**14**) could function as well as a dim, but more sensitive dye (**13**). Both poRhoVR **13** (Figure S4a–c) and **14** (Figure 3a–c) localize well to cellular membranes and readily report on spontaneously-firing action potentials in single-trial acquisitions, revealing a range of neuronal firing rates similar to previously reported ranges.⁶⁴ In some cases, poRhoVR **14** clearly visualizes sub-threshold voltage dynamics, likely postsynaptic potentials (Figure 3c, cell 3, asterisks).

Consistent with its performance in HEK cells, poRhoVR **14** was approximately 8 to 12-fold brighter than **13** under identical experimental conditions (Figure S5a). In a complementary fashion, the F/F value per spike/action potential for **13** was larger than for **14** (12% vs 6%, Figure S5b) but with lower overall signal-to-noise ratio (SNR, 20:1 vs 40:1, Figure S5c). Because of the higher brightness and SNR for detecting action potentials, we used poRhoVR **14** for subsequent experiments.

We next examined the photostability, internalization rate, and toxicity of poRhoVR **14**. The photostability of poRhoVR **14** is comparable to the photostability of the previously-reported BeRST 1 (Figure S6).³⁹ We also measured the persistence of poRhoVR **14** on the cell membrane in HEK cells. We examined the degree of poRhoVR **14** internalization from the membrane by measuring the colocalization between calcein-AM⁶⁵ fluorescence – a cytosolic stain that becomes fluorescent and is retained in living cells – and poRhoVR **14** (Figure S7). Increased colocalization values indicates a higher degree of internalization of the membrane-associated poRhoVR **14**. We find a low degree of colocalization between poRhoVR **14** signal and cytosolic calcein-AM after an initial 20 minutes of loading (the Pearson's correlation coefficient is 0.22 ± 0.2 , mean \pm S.E.M. for $n = 3$ coverslips) (Figure S7a). There is an increase in the degree of colocalization, to approximately 0.26, after additional observation for up to 2 hours (Figure S7), but the changes are not statistically significant ($P > 0.05$, Dunnett's multiple comparisons test, see Figure S7). Finally, we examined the toxicity of poRhoVR **14** in HEK293T cells using calcein-AM. Comparison of the colocalization of Hoechst 33342 fluorescence, which stains the nuclei of both dead and live cells, and calcein-AM fluorescence reveals no difference in colocalization, and therefore toxicity, between vehicle-treated HEK293T cells (DMSO) and up to 5 μ M poRhoVR **14** (Figure S8).

poRhoVR **14** and optogenetic activator ChR2

poRhoVR **14** can be used in multicolor experiments, not only for tracking static fluorescence associated with distinct organelles (Figure 2a–d), but also in concert with

commonly employed optogenetic actuators and sensors. We expressed the blue light-activated opsin, ChannelRhodopsin-2 (ChR2),^{66–67} fused to yellow fluorescent protein (YFP) in a subset of hippocampal neurons isolated from rat (Figure 4a and b). Bath application of poRhoVR **14** to these same neurons results in membrane-localized fluorescence (Figure 4c) that is spectrally isolated from the YFP signal (Figure 4d).

The combined use of ChR and poRhoVR allows dissection of functional connectivity across a large number of neurons. Optical stimulation of cell 1 (475 nm, 5 ms, 1.92 mW/mm²) results in ChR2-evoked action potentials optically recorded at cell 1 (Figure 4e and f). Cells 4 and 5 appear monosynaptically coupled to ChR2-positive cell 1 with action potential latencies of 6.7 ms ± 1.5 ms (S.D. n = 60 pairs of spikes) and 5.6 ms ± 1.3 ms (S.D., n = 20 out of 60 spikes), respectively. However, the data reveals differences in the relative strengths of these connections with cell 1 triggering firing in cell 4 for 100% of action potentials, and only 33% for cell 5. Interestingly, bursts of spontaneous activity indicate strong recurrent connectivity between all neurons (Figure 4e and f, grey shaded areas), but firing initiated in the ChR2-expressing neuron (cell 1, Figure 4a–d) activates only a subset of these neurons (Figure 4e and f): notably, cell 4, nearly 50 μm away from cell 1, and cell 5, over 120 μm distant from ChR2-expressing cell 1.

The combination of poRhoVR and ChR2 enables interrogation of sub-threshold potentials. In a few cases, during cyan light stimulation, we observe slower, sub-threshold potentials in cells up to 400 microns away from the ChR2-expressing neuron (Figure S9d and e, cells 2 – 4, asterisks), highlighting the ability of poRhoVR **14** to monitor sub-threshold voltage changes (Figure 3a–c). The use of cyan light to stimulate ChR2 does not cross-excite poRhoVR **14**, as indicated by the lack of stimulus artifact in the ChR2-negative cells in the same field of view (Figure 4d and e, Figure S9). Together, these experiments establish poRhoVR **14** as a powerful complement for all-optical electrophysiology utilizing NIR absorbing indicators.

Two color imaging with poRhoVR **14** and Ca²⁺ indicators

In addition to deployment alongside light-activated actuators, poRhoVR can be used with optical indicators. Fluorescent sensors for Ca²⁺ are among the most widely used optical sensors. Despite some three decades since the initial reports of fluorescent indicators for this critical intracellular messenger,^{68–69} most Ca²⁺ indicators utilize excitation and emission profiles firmly centered in the blue/green region of the visible spectrum (for example, Oregon Green BAPTA, OGB,⁷⁰ and the GCaMP family of genetically encoded indicators).⁷¹ Although promising new Ca²⁺ indicators, both synthetic^{72–75} and genetically encoded,^{76–79} possess red-shifted excitation and emission spectra, circularly-permuted (cp) GFP-based indicators, like the GCaMP family,⁷¹ dominate the landscape of functional imaging.^{80–81} Therefore, fluorescent voltage indicators with orthogonal wavelengths are required.

We performed two-color, simultaneous voltage and Ca²⁺ imaging in the same cells using poRhoVR **14** and the synthetic Ca²⁺ indicator, OGB (Figure 5a–c). We treated hippocampal neurons with both poRhoVR **14** (500 nM) and OGB (1 μM) simultaneously and imaged using an image-splitting device to project two emission wavelengths onto the same camera chip. Under these conditions, we observe clear membrane-associated fluorescence for

poRhoVR **14** (Figure 5a) and cytosolic fluorescence for OGB (Figure 5b). We established that no cross-excitation exists under these conditions (Figure S10). Using field-stimulation electrodes, we evoked a series of 10 action potentials, across a range of frequencies, and simultaneously recorded voltage (Figure 5c, magenta traces) and Ca^{2+} (Figure 5c, green traces) dynamics.

Both poRhoVR **14** and OGB clearly resolve single action potentials when activity is evoked at rates of either 5 or 10 Hz. poRhoVR **14** clearly resolves action potentials at firing rates of 20 and 30 Hz (Figure 5c). OGB, despite its fast Ca^{2+} response kinetics (<5 ms to action potential peak)⁷¹ compared to GCaMP6f (~45 ms to peak)⁷¹ and other genetically encoded indicators,^{82–84} fails to accurately report individual action potential-evoked Ca^{2+} transients at firing frequencies higher than 10 Hz (Figure 5c). Neurons in the brain and retina can fire action potentials at rates up to several hundred Hz, for example in interneurons of the hippocampus,⁸⁵ Purkinje cells of the cerebellum,⁸⁶ and ganglion cells of the retina,⁸⁷ emphasizing the need for indicators with fast response kinetics.

Ca^{2+} indicators are often characterized against varying numbers of action potentials arriving at a constant frequency. However, neural information is often encoded in the form of spike rates. Therefore, resolution of individual spikes and firing frequency is critical for understanding the underlying physiology of the system under observation. Even with very fast OGB, estimating spike frequency using Ca^{2+} imaging traces alone was unsuccessful. Neither peak Ca^{2+} F/F (Figure S11a) nor integrated area under the curve (Figure S11b) were able to resolve differences at 5, 10, 20, or 30 Hz firing rates. In contrast, the optically recorded voltage transients revealed by poRhoVR **14** clearly discriminates between firing frequencies of 5, 10, 20, and 30 Hz (Figure S11c).

Simultaneous voltage and Ca^{2+} imaging in the same cells can also be achieved alongside genetically encoded indicators, like GCaMP6. We again stained neurons with poRhoVR **14** (1 μM). This time, a subset of hippocampal neurons expressed GCaMP6s. Again, poRhoVR localizes to membranes (Figure 5d), while GCaMP6s fluorescence appears cytosolic (Figure 5e). Simultaneous voltage and Ca^{2+} imaging of spontaneous activity in hippocampal neurons reveals fast-spiking bursts resolved in voltage (Figure 5f–h, magenta trace), followed by slower, sustained increases in GCaMP6-associated fluorescence (Figure 5f–h, green trace). Notably, voltage imaging with poRhoVR **14** exhibits sufficiently high temporal resolution to distinguish individual action potentials in spike volleys (Figure 5g, 8 spikes; Figure 5h, 9 spikes), while Ca^{2+} imaging does not. Together, these experiments establish the utility of poRhoVR dyes for monitoring fast spiking in neurons alongside commonly used synthetic and genetically-encoded Ca^{2+} indicators and emphasizes the care needed when interpreting Ca^{2+} imaging data.

Voltage and Ca^{2+} imaging and electrode recording in a mouse model of retina degeneration

The NIR (>700 nm) excitation and emission spectra of poRhoVR dyes, along with their good voltage sensitivity, compatibility with commonly used optogenetic sensors and actuators, and ready uptake into cell membranes (Figure S12) makes poRhoVR **14** a promising candidate for mapping voltage dynamics in intact neural tissue like retinas. The

retina is a highly organized and accessible outpost of the central nervous system. Light responses initiated in rods and cones are synaptically transmitted to bipolar cells, which activate retinal ganglion cells (RGCs). RGCs generate the action potentials that carry visual information to the brain. In normally functioning retinas, the intrinsic light sensitivity of photoreceptors in rods and cones complicates optical imaging of both voltage and Ca^{2+} transients in RGCs, because visible light (or high intensity two photon excitation) used to excite the indicators triggers physiological responses.⁸⁸ We applied poRhoVR **14** to investigate membrane potential dynamics in retinas from a mouse model of retina degeneration.

In particular, retinas from *rd1* mice are an attractive model system in which functional imaging can be applied to explore mechanisms occurring in inherited visual disorders, including the degenerative disorder retinitis pigmentosa (RP).⁸⁹ Lacking a functional β subunit of rod cGMP phosphodiesterase (βPDE),⁹⁰ *rd1* mice suffer rapid loss of rod cells, followed by a delayed loss of cone cells. As a result, these mice lack rods and cones and are therefore blind, yet still retain functional RGCs in the ganglion cell layer (GCL). Therefore, apart from the rare melanopsin-expressing, intrinsically sensitive RGC (<2% of the RGCs) the surviving RGCs in *rd1* retinas have no light response and continue to receive synaptic input from bipolar cells. RGCs in *rd1* mice develop hyperactivity, firing spontaneous bursts of spikes in darkness. This phenomenon has been observed only through electrophysiological recordings that sample only a fraction of cells, or by Ca^{2+} imaging with GCaMP expressed in RGCs, which is indirect and has low temporal resolution.^{87, 91}

The precise mechanisms underlying hyperactivity are not understood, and voltage imaging could reveal where in the retinal circuitry this activity originates and how it propagates from neuron to neuron.

To explore the interplay between neuronal voltage and Ca^{2+} signaling in this model of retinopathy, we prepared *ex vivo*, flat-mount retinas from *rd1* mice that express GCaMP6f in retinal ganglion cells (RGCs). Bath application of poRhoVR **14** (5 μM , in oxygenated ACSF) results in diffuse poRhoVR **14** staining throughout the tissue, as assessed by widefield fluorescence microscopy (Figure 6a, Figure S14d–e). In retinas from *rd1* mice, we observed spontaneous oscillations of poRhoVR **14** fluorescence (Figure 6d–h, magenta traces). To confirm that these changes in poRhoVR **14** dynamics correspond to voltage changes in RGCs, we paired voltage imaging with multi-electrode array (MEA) recordings of extracellular potential.

The poRhoVR-stained retinas were mounted on a 64-channel MEA to simultaneously record transmembrane potential (poRhoVR **14**), extracellular potential (MEA), and Ca^{2+} transients (GCaMP6f) in many RGCs. Simultaneous transmembrane voltage imaging and MEA recording of extracellular potentials (black traces) confirms that poRhoVR **14** (magenta traces) accurately reports changes in transmembrane potential in RGCs of the retina (Figure 6c–f). The time courses of the MEA signals (black) and poRhoVR **14** signals (magenta) match well, establishing that poRhoVR senses voltage changes in mouse retina. The signs of the MEA and poRhoVR **14** signals are inversely related (Figure 6c–f): poRhoVR **14** measures transmembrane potential, while MEA records extracellular potentials. A zoomed-

in view of poRhoVR **14** and MEA signals (Figure 6g and h), where the black MEA signals have been inverted to enable better comparisons, show excellent correspondence between the optically recorded transmembrane potential measured with poRhoVR **14** (magenta) and the MEA recording (black).

Voltage imaging reveals spontaneous membrane potential depolarizations that appear clustered in bursts throughout the imaging session (Figure 6c and d, magenta). These optically-recorded oscillatory bursts are, to our knowledge, the first direct imaging of membrane potential dynamics in *rd1* retinas, and are consistent with previous MEA recordings in *rd1* retinas.^{92–93} GCaMP6f recordings from the same areas revealed slower, Ca²⁺ transients that were delayed relative to increases in the transmembrane potential measured by poRhoVR **14** fluorescence (Figure 6c and d, green). This lag between Ca²⁺ and voltage is similar to our observations of simultaneous Ca²⁺ / voltage imaging in hippocampal neurons (Figure 5d–h) and provides the first direct and simultaneous observation of voltage and Ca²⁺ in the mouse retina. We observe no evidence of oxidative photobleaching⁹⁴ of po-rhodamines under these imaging conditions (Figure S13).

Voltage imaging with poRhoVR **14** enables dissection of the temporal evolution of neuronal activity in *rd1* retina. Synaptic isolation of RGCs via blockade of all major forms of excitatory and inhibitory synaptic transmission results in evolution of activity from short, unsynchronized firing patterns (Figure 6c, d, and g) to synchronous and sustained firing (Figure 6e, f, and h), consistent with the idea that the driver of this behavior is presynaptic.⁹² Voltage imaging with poRhoVR **14** also allows investigation of the spatial differences in voltage dynamics with the retina. We recorded fluorescence from a region of interest (ROI) composed of a ring with a width approximately matching that of an RGC (~10 μm) around the MEA electrode (Figure 6a and b). This enables a direct comparison to extracellular potentials recorded by the MEA (Figure 6c and d, black). For the two electrodes visible in the recording image (Figure 6a and b), the MEA recording is closely matched by the poRhoVR **14** dynamics (Figure 6c and d, black vs. magenta). The use of poRhoVR **14** allows examination of the spatial relationships of voltage changes at locations distant from electrodes (Figure S14). Imaging of poRhoVR **14** signals recorded in ROIs in between electrodes reveal a unique activity profile that is not fully recapitulated by ROIs near the respective electrodes (Figure S14a–b), highlighting the ability of poRhoVR to map the spatial extent of voltage dynamics in retina. This methodology could prove a promising starting point for mapping the dendritic fields of RGCs by probing where voltage dynamics become convoluted with additional signals.

Conclusion

In summary, we present the design, synthesis, and application of phosphine-oxide rhodamines for voltage imaging. These new poRhoVRs have excitation and emission profiles above 700 nm and possess good voltage sensitivity. Their compatibility with other optical sensors and actuators makes them a powerful complement to existing approaches to dissect neuronal activity. We show that poRhoVR **14** can report on spontaneous action potentials in rat hippocampal neurons and enables all-optical electrophysiological manipulations with Chr2. Simultaneous voltage imaging with poRhoVR **14** alongside either

fast synthetic Ca²⁺ indicators or genetically encoded Ca²⁺ indicators reveals the difficulty of relying solely on Ca²⁺ imaging to interpret underlying neuronal activity. Furthermore, poRhoVR **14** can be deployed in intact retinas alongside multi-electrode arrays and Ca²⁺ imaging to record from many RGCs at once in a mouse model of retinal degeneration, providing a first direct visualization of voltage dynamics alongside simultaneous Ca²⁺ imaging in the retina.

In the future, we envision combining poRhoVR with chemical-genetic hybrid methods to enable cell type-specific labelling in intact tissues.^{95–96} Beyond the chemical sensing presented in this manuscript, innovations in microscopy will be needed to achieve the kilohertz framerates, with micrometer resolution, across large, 3D volumes regions of the central nervous system that will be required for visualizing patterns of activity in arrays of neurons *in vivo*.⁹⁷ Promising advances microscopy,⁹ including light sheet and swept-field microscopy,⁹⁸ redesigned optical paths,⁹⁹ holographic imaging,^{100–101} and compressive sensing¹⁰² hint at possible avenues towards the use of poRhoVR for *in vivo* brain imaging.

Supplementary Material

Refer to Web version on PubMed Central for supplementary material.

ACKNOWLEDGMENT

Research in the Miller lab is supported by grants from the NIH (R01NS098088, R35GM119855) and Klingenstein-Simon Foundations (40746). E.W.M and R.H.K. acknowledge support from NSF Neuronex (1707350). M.A.G. was supported in part by a training grant from the NIH (T32GM066698). Crystallographic data was acquired on an ApexII-Quazar, supported NIH grant S10RR027172. Research in the Kramer lab is supported by the NIH (R01EY024334 and R01NS100911). We thank Benjamin Smith for assistance with image analysis.

REFERENCES

1. Huang B; Babcock H; Zhuang X, Breaking the Diffraction Barrier: Super-Resolution Imaging of Cells. *Cell* 2010, 143 (7), 1047–1058. [PubMed: 21168201]
2. Power RM; Huisken J, A guide to light-sheet fluorescence microscopy for multiscale imaging. *Nature Methods* 2017, 14, 360. [PubMed: 28362435]
3. Richardson DS; Lichtman JW, Clarifying Tissue Clearing. *Cell* 2015, 162 (2), 246–257. [PubMed: 26186186]
4. Hirayama T; Van de Bittner GC; Gray LW; Lutsenko S; Chang CJ, Near-infrared fluorescent sensor for *in vivo* copper imaging in a murine Wilson disease model. *Proceedings of the National Academy of Sciences* 2012, 109 (7), 2228–2233.
5. Chung K; Wallace J; Kim S-Y; Kalyanasundaram S; Andalman AS; Davidson TJ; Mirzabekov JJ; Zalocusky KA; Mattis J; Denisin AK; Pak S; Bernstein H; Ramakrishnan C; Grosenick L; Gradinaru V; Deisseroth K, Structural and molecular interrogation of intact biological systems. *Nature* 2013, 497, 332. [PubMed: 23575631]
6. Weissleder R, A clearer vision for *in vivo* imaging. *Nature Biotechnology* 2001, 19, 316–317.
7. Friebe M; Helfmann J; Netz UJ; Meinke MC, Influence of oxygen saturation on the optical scattering properties of human red blood cells in the spectral range 250 to 2000 nm. *Journal of Biomedical Optics* 2009, 14 (3), 1–6, 6.
8. Tsien RY, Imagining imaging's future. *Nature reviews. Molecular cell biology* 2003, Suppl, Ss16–21.
9. Lecoq J; Orlova N; Grewe BF, Wide. Fast. Deep: Recent Advances in Multiphoton Microscopy of *In Vivo* Neuronal Activity. *The Journal of Neuroscience* 2019, 39 (46), 9042–9052. [PubMed: 31578235]

10. Fabian J; Nakazumi H; Matsuoka M, Near-infrared absorbing dyes. *Chemical Reviews* 1992, 92 (6), 1197–1226.
11. Alfano RR; Demos SG; Gayen SK, Advances in Optical Imaging of Biomedical Media. *Annals of the New York Academy of Sciences* 1997, 820 (1), 248–271. [PubMed: 9237460]
12. Tung C-H; Lin Y; Moon WK; Weissleder R, A Receptor-Targeted Near-Infrared Fluorescence Probe for In Vivo Tumor Imaging. *ChemBioChem* 2002, 3 (8), 784–786. [PubMed: 12203978]
13. Frangioni JV, In vivo near-infrared fluorescence imaging. *Current Opinion in Chemical Biology* 2003, 7 (5), 626–634. [PubMed: 14580568]
14. Cosco ED; Caram JR; Bruns OT; Franke D; Day RA; Farr EP; Bawendi MG; Sletten EM, Flavylium Polymethine Fluorophores for Near- and Shortwave Infrared Imaging. *Angewandte Chemie International Edition* 2017, 56 (42), 13126–13129. [PubMed: 28806473]
15. Hilderbrand SA; Weissleder R, Near-infrared fluorescence: application to in vivo molecular imaging. *Current Opinion in Chemical Biology* 2010, 14 (1), 71–79. [PubMed: 19879798]
16. Kubo Y; Watanabe K; Nishiyabu R; Hata R; Murakami A; Shoda T; Ota H, Near-Infrared Absorbing Borondibenzopyrromethenes that Serve As Light-Harvesting Sensitizers for Polymeric Solar Cells. *Organic Letters* 2011, 13 (17), 4574–4577. [PubMed: 21827161]
17. Liu P; Gao F; Zhou L; Chen Y; Chen Z, Tetrathienyl-functionalized red- and NIR-absorbing BODIPY dyes appending various peripheral substituents. *Organic & Biomolecular Chemistry* 2017, 15 (6), 1393–1399. [PubMed: 28101544]
18. Kubota Y; Kimura K; Jin J; Manseki K; Funabiki K; Matsui M, Synthesis of near-infrared absorbing and fluorescing thiophene-fused BODIPY dyes with strong electron-donating groups and their application in dye-sensitized solar cells. *New Journal of Chemistry* 2019, 43 (3), 1156–1165.
19. Koide Y; Urano Y; Hanaoka K; Piao W; Kusakabe M; Saito N; Terai T; Okabe T; Nagano T, Development of NIR Fluorescent Dyes Based on Si-rhodamine for in Vivo Imaging. *Journal of the American Chemical Society* 2012, 134 (11), 5029–5031. [PubMed: 22390359]
20. Azuma E; Nakamura N; Kuramochi K; Sasamori T; Tokitoh N; Sagami I; Tsubaki K, Exhaustive Syntheses of Naphthofluoresceins and Their Functions. *The Journal of Organic Chemistry* 2012, 77 (7), 3492–3500. [PubMed: 22428609]
21. Lee LG; Berry GM; Chen C-H, Vita blue: A new 633-nm excitable fluorescent dye for cell analysis. *Cytometry* 1989, 10 (2), 151–164. [PubMed: 2714106]
22. Yuan L; Lin W; Zhao S; Gao W; Chen B; He L; Zhu S, A Unique Approach to Development of Near-Infrared Fluorescent Sensors for in Vivo Imaging. *Journal of the American Chemical Society* 2012, 134 (32), 13510–13523. [PubMed: 22816866]
23. Sibrian-Vazquez M; Escobedo JO; Lowry M; Fronczek FR; Strongin RM, Field Effects Induce Bathochromic Shifts in Xanthene Dyes. *Journal of the American Chemical Society* 2012, 134 (25), 10502–10508. [PubMed: 22642754]
24. Gorka AP; Nani RR; Schnermann MJ, Harnessing Cyanine Reactivity for Optical Imaging and Drug Delivery. *Accounts of Chemical Research* 2018, 51 (12), 3226–3235. [PubMed: 30418020]
25. Grimm JB; Sung AJ; Legant WR; Hulamm P; Matlosz SM; Betzig E; Lavis LD, Carbofluoresceins and Carborhodamines as Scaffolds for High-Contrast Fluorogenic Probes. *ACS Chemical Biology* 2013, 8 (6), 1303–1310. [PubMed: 23557713]
26. Grimm JB; Gruber TD; Ortiz G; Brown TA; Lavis LD, Virginia Orange: A Versatile, Red-Shifted Fluorescein Scaffold for Single- and Dual-Input Fluorogenic Probes. *Bioconjugate Chemistry* 2016, 27 (2), 474–480. [PubMed: 26636613]
27. Ortiz G; Liu P; Naing SHH; Muller VR; Miller EW, Synthesis of Sulfonated Carbofluoresceins for Voltage Imaging. *J Am Chem Soc* 2019, 141 (16), 6631–6638. [PubMed: 30978010]
28. Fu M; Xiao Y; Qian X; Zhao D; Xu Y, A design concept of long-wavelength fluorescent analogs of rhodamine dyes: replacement of oxygen with silicon atom. *Chemical Communications* 2008, (15), 1780–1782. [PubMed: 18379691]
29. Koide Y; Urano Y; Hanaoka K; Terai T; Nagano T, Evolution of Group 14 Rhodamines as Platforms for Near-Infrared Fluorescence Probes Utilizing Photoinduced Electron Transfer. *ACS Chemical Biology* 2011, 6 (6), 600–608. [PubMed: 21375253]

30. Pastierik T; Šebej P; Medalová J; Štacko P; Klán P, Near-Infrared Fluorescent 9-Phenylethynylpyronin Analogues for Bioimaging. *The Journal of Organic Chemistry* 2014, 79 (8), 3374–3382. [PubMed: 24684518]
31. Liu J; Sun Y-Q; Zhang H; Shi H; Shi Y; Guo W, Sulfone-Rhodamines: A New Class of Near-Infrared Fluorescent Dyes for Bioimaging. *ACS Applied Materials & Interfaces* 2016, 8 (35), 22953–22962. [PubMed: 27548811]
32. Zhou X; Lai R; Beck JR; Li H; Stains CI, Nebraska Red: a phosphinate-based near-infrared fluorophore scaffold for chemical biology applications. *Chemical Communications* 2016, 52 (83), 12290–12293. [PubMed: 27709196]
33. Chai X; Cui X; Wang B; Yang F; Cai Y; Wu Q; Wang T, Near-Infrared Phosphorus-Substituted Rhodamine with Emission Wavelength above 700 nm for Bioimaging. *Chemistry – A European Journal* 2015, 21 (47), 16754–16758.
34. Grzybowski M; Taki M; Senda K; Sato Y; Ariyoshi T; Okada Y; Kawakami R; Imamura T; Yamaguchi S, A Highly Photostable Near-Infrared Labeling Agent Based on a Phosphorhodamine for Long-Term and Deep Imaging. *Angewandte Chemie International Edition* 2018, 57 (32), 10137–10141. [PubMed: 29984448]
35. Sasaki E; Kojima H; Nishimatsu H; Urano Y; Kikuchi K; Hirata Y; Nagano T, Highly Sensitive Near-Infrared Fluorescent Probes for Nitric Oxide and Their Application to Isolated Organs. *Journal of the American Chemical Society* 2005, 127 (11), 3684–3685. [PubMed: 15771488]
36. Zhang Z; Achilefu S, Design, synthesis and evaluation of near-infrared fluorescent pH indicators in a physiologically relevant range. *Chemical Communications* 2005, (47), 5887–5889. [PubMed: 16317464]
37. Kiyose K; Kojima H; Urano Y; Nagano T, Development of a Ratiometric Fluorescent Zinc Ion Probe in Near-Infrared Region, Based on Tricarbocyanine Chromophore. *Journal of the American Chemical Society* 2006, 128 (20), 6548–6549. [PubMed: 16704241]
38. Kulkarni RU; Yin H; Pourmandi N; James F; Adil MM; Schaffer DV; Wang Y; Miller EW, A Rationally Designed, General Strategy for Membrane Orientation of Photoinduced Electron Transfer-Based Voltage-Sensitive Dyes. *ACS Chem Biol* 2017, 12 (2), 407–413. [PubMed: 28004909]
39. Huang YL; Walker AS; Miller EW, A Photostable Silicon Rhodamine Platform for Optical Voltage Sensing. *J Am Chem Soc* 2015, 137 (33), 10767–76. [PubMed: 26237573]
40. Deal PE; Kulkarni RU; Al-Abdullatif SH; Miller EW, Isomerically Pure Tetramethylrhodamine Voltage Reporters. *J Am Chem Soc* 2016, 138 (29), 9085–8. [PubMed: 27428174]
41. Shoham D; Glaser DE; Arieli A; Kenet T; Wijnbergen C; Toledo Y; Hildesheim R; Grinvald A, Imaging cortical dynamics at high spatial and temporal resolution with novel blue voltage-sensitive dyes. *Neuron* 1999, 24 (4), 791–802. [PubMed: 10624943]
42. Matiukas A; Mitrea BG; Pertsov AM; Wuskell JP; Wei M.-d.; Watras J; Millard AC; Loew LM, New near-infrared optical probes of cardiac electrical activity. *American Journal of Physiology-Heart and Circulatory Physiology* 2006, 290 (6), H2633–H2643. [PubMed: 16399869]
43. Yan P; Acker CD; Zhou W-L; Lee P; Bollensdorff C; Negrean A; Lotti J; Sacconi L; Antic SD; Kohl P; Mansvelder HD; Pavone FS; Loew LM, Palette of fluorinated voltage-sensitive hemicyanine dyes. *Proceedings of the National Academy of Sciences* 2012, 109 (50), 20443–20448.
44. Treger Jeremy S.; Priest Michael F.; Iezzi R; Bezanilla F, Real-Time Imaging of Electrical Signals with an Infrared FDA-Approved Dye. *Biophysical Journal* 2014, 107 (6), L09–L12. [PubMed: 25229155]
45. Hochbaum DR; Zhao Y; Farhi SL; Klapoetke N; Werley CA; Kapoor V; Zou P; Kralj JM; Maclaurin D; Smedemark-Margulies N; Saulnier JL; Boulting GL; Straub C; Cho YK; Melkonian M; Wong GK-S; Harrison DJ; Murthy VN; Sabatini BL; Boyden ES; Campbell RE; Cohen AE, All-optical electrophysiology in mammalian neurons using engineered microbial rhodopsins. *Nature Methods* 2014, 11, 825. [PubMed: 24952910]
46. Monakhov M; Matlashov M; Colavita M; Song C; Shcherbakova DM; Antic SD; Verkhusha V; Knopfel T, Bright near-infrared genetically encoded voltage indicator for all-optical electrophysiology. *bioRxiv* 2019, 536359.

47. Kannan M; Vasan G; Huang C; Haziza S; Li JZ; Inan H; Schnitzer MJ; Pieribone VA, Fast, in vivo voltage imaging using a red fluorescent indicator. *Nature Methods* 2018, 15 (12), 1108–1116. [PubMed: 30420685]
48. Zhou X; Fang Y; Lesiak L; Stains CI, A Phosphinate-Containing Fluorophore Capable of Selectively Inducing Apoptosis in Cancer Cells. *ChemBioChem* 2019, 20 (13), 1712–1716. [PubMed: 30753755]
49. Bandichhor R; Petrescu AD; Vespa A; Kier AB; Schroeder F; Burgess K, Synthesis of a New Water-Soluble Rhodamine Derivative and Application to Protein Labeling and Intracellular Imaging. *Bioconjugate Chemistry* 2006, 17 (5), 1219–1225. [PubMed: 16984131]
50. Nadler A; Yushchenko DA; Müller R; Stein F; Feng S; Mülle C; Carta M; Schultz C, Exclusive photorelease of signalling lipids at the plasma membrane. *Nature Communications* 2015, 6, 10056.
51. Kulkarni RU; Vandenberghe M; Thunemann M; James F; Andreassen OA; Djurovic S; Devor A; Miller EW, In Vivo Two-Photon Voltage Imaging with Sulfonated Rhodamine Dyes. *ACS Cent Sci* 2018, 4 (10), 1371–1378. [PubMed: 30410975]
52. Tan B; Tchatchoua CN; Dong L; McGrath JE, Synthesis and characterization of arylene ether imide reactive oligomers and polymers containing diaryl alkyl phosphine oxide groups. *Polym Advan Technol* 1998, 9 (1), 84–93.
53. Kovi R; Nampalli S; Tharial Peter X Process For Preparation Of Isosulfan Blue. US 2008/0281127 A1, 2007/05/11, 2008.
54. Kulkarni RU; Vandenberghe M; Thunemann M; James F; Andreassen OA; Djurovic S; Devor A; Miller EW, In Vivo Two-Photon Voltage Imaging with Sulfonated Rhodamine Dyes. *ACS Central Science* 2018, 4 (10), 1371–1378. [PubMed: 30410975]
55. Mudd G; Pi IP; Fethers N; Dodd PG; Barbeau OR; Auer M, A general synthetic route to isomerically pure functionalized rhodamine dyes. *Methods and Applications in Fluorescence* 2015, 3 (4), 045002. [PubMed: 29148510]
56. Schindelin J; Arganda-Carreras I; Frise E; Kaynig V; Longair M; Pietzsch T; Preibisch S; Rueden C; Saalfeld S; Schmid B; Tinevez J-Y; White DJ; Hartenstein V; Eliceiri K; Tomancak P; Cardona A, Fiji: an open-source platform for biological-image analysis. *Nature Methods* 2012, 9 (7), 676–682. [PubMed: 22743772]
57. Johnson LV; Walsh ML; Chen LB, Localization of mitochondria in living cells with rhodamine 123. *Proceedings of the National Academy of Sciences* 1980, 77 (2), 990–994.
58. Cooksey CJ, Quirks of dye nomenclature. 5. Rhodamines. *Biotechnic & Histochemistry* 2016, 91 (1), 71–76. [PubMed: 26529223]
59. Latt SA; Stetten G, Spectral studies on 33258 Hoechst and related bisbenzimidazole dyes useful for fluorescent detection of deoxyribonucleic acid synthesis. *Journal of Histochemistry & Cytochemistry* 1976, 24 (1), 24–33. [PubMed: 943439]
60. Homma R; Baker BJ; Jin L; Garaschuk O; Konnerth A; Cohen LB; Zecevic D, Wide-field and two-photon imaging of brain activity with voltage- and calcium-sensitive dyes. *Philosophical transactions of the Royal Society of London. Series B, Biological sciences* 2009, 364 (1529), 2453–67. [PubMed: 19651647]
61. Xu Y; Zou P; Cohen AE, Voltage imaging with genetically encoded indicators. *Curr Opin Chem Biol* 2017, 39, 1–10. [PubMed: 28460291]
62. Sjulson L; Miesenböck G, Optical recording of action potentials and other discrete physiological events: a perspective from signal detection theory. *Physiology (Bethesda, Md.)* 2007, 22, 47–55.
63. Wilt Brian A.; Fitzgerald James E.; Schnitzer Mark J., Photon Shot Noise Limits on Optical Detection of Neuronal Spikes and Estimation of Spike Timing. *Biophysical Journal* 2013, 104 (1), 51–62. [PubMed: 23332058]
64. Walker AS; Raliski BK; Karbasi K; Zhang P; Sanders K; Miller EW, Optical spike detection and connectivity analysis with a far-red voltage-sensitive fluorophore reveals changes to network connectivity in development and disease. *bioRxiv* 2020, 2020.10.09.332270.
65. Johnson ID, *Molecular Probes Handbook: A Guide to Fluorescent Probes and Labeling Technologies*. Life Technologies Corporation: 2010.

66. Nagel G; Szellas T; Huhn W; Kateriya S; Adeishvili N; Berthold P; Ollig D; Hegemann P; Bamberg E, Channelrhodopsin-2, a directly light-gated cation-selective membrane channel. *Proc Natl Acad Sci U S A* 2003, 100 (24), 13940–5. [PubMed: 14615590]
67. Boyden ES; Zhang F; Bamberg E; Nagel G; Deisseroth K, Millisecond-timescale, genetically targeted optical control of neural activity. *Nature Neuroscience* 2005, 8 (9), 1263–1268. [PubMed: 16116447]
68. Grynkiewicz G; Poenie M; Tsien RY, A new generation of Ca²⁺ indicators with greatly improved fluorescence properties. *J Biol Chem* 1985, 260 (6), 3440–50. [PubMed: 3838314]
69. Minta A; Kao JP; Tsien RY, Fluorescent indicators for cytosolic calcium based on rhodamine and fluorescein chromophores. *J Biol Chem* 1989, 264 (14), 8171–8. [PubMed: 2498308]
70. Gee KR; Poot M; Klaubert DH; Sun W-C; Haugland RP; Mao F Fluorinated xanthene derivatives as fluorescent dyes and their use in staining biological materials. WO9739064A1, 1997.
71. Chen T-W; Wardill TJ; Sun Y; Pulver SR; Renninger SL; Baohan A; Schreiter ER; Kerr RA; Orger MB; Jayaraman V; Looger LL; Svoboda K; Kim DS, Ultrasensitive fluorescent proteins for imaging neuronal activity. *Nature* 2013, 499, 295. [PubMed: 23868258]
72. Egawa T; Hirabayashi K; Koide Y; Kobayashi C; Takahashi N; Mineno T; Terai T; Ueno T; Komatsu T; Ikegaya Y; Matsuki N; Nagano T; Hanaoka K, Red fluorescent probe for monitoring the dynamics of cytoplasmic calcium ions. *Angew Chem Int Ed Engl* 2013, 52 (14), 3874–7. [PubMed: 23440861]
73. Diwu Z; Guo H; Peng R; Zhao Q; Liu J; Liao J Carbofluorescein lactone metal ion indicators and their applications. US20140378344A1, 2014.
74. Collot M; Wilms CD; Bentkhayet A; Marcaggi P; Couchman K; Charpak S; Dieudonne S; Hausser M; Feltz A; Mallet JM, CaRuby-Nano: a novel high affinity calcium probe for dual color imaging. *Elife* 2015, 4, e05808.
75. Ogasawara H; Grzybowski M; Hosokawa R; Sato Y; Taki M; Yamaguchi S, A far-red fluorescent probe based on a phospho-fluorescein scaffold for cytosolic calcium imaging. *Chemical Communications* 2018, 54 (3), 299–302. [PubMed: 29239411]
76. Zhao Y; Araki S; Wu J; Teramoto T; Chang Y-F; Nakano M; Abdelfattah AS; Fujiwara M; Ishihara T; Nagai T; Campbell RE, An Expanded Palette of Genetically Encoded Ca²⁺ Indicators. *Science* 2011, 333 (6051), 1888–1891. [PubMed: 21903779]
77. Dana H; Mohar B; Sun Y; Narayan S; Gordus A; Hasseman JP; Tsegaye G; Holt GT; Hu A; Walpita D; Patel R; Macklin JJ; Bargmann CI; Ahrens MB; Schreiter ER; Jayaraman V; Looger LL; Svoboda K; Kim DS, Sensitive red protein calcium indicators for imaging neural activity. *eLife* 2016, 5, e12727. [PubMed: 27011354]
78. Inoue M; Takeuchi A; Manita S; Horigane S.-i.; Sakamoto M; Kawakami R; Yamaguchi K; Otomo K; Yokoyama H; Kim R; Yokoyama T; Takemoto-Kimura S; Abe M; Okamura M; Kondo Y; Quirin S; Ramakrishnan C; Imamura T; Sakimura K; Nemoto T; Kano M; Fujii H; Deisseroth K; Kitamura K; Bito H, Rational Engineering of XCaMPs, a Multicolor GECI Suite for In Vivo Imaging of Complex Brain Circuit Dynamics. *Cell* 2019, 177 (5), 1346–1360.e24. [PubMed: 31080068]
79. Qian Y; Piatkevich KD; Mc Larney B; Abdelfattah AS; Mehta S; Murdock MH; Gottschalk S; Molina RS; Zhang W; Chen Y; Wu J; Drobizhev M; Hughes TE; Zhang J; Schreiter ER; Shoham S; Razansky D; Boyden ES; Campbell RE, A genetically encoded near-infrared fluorescent calcium ion indicator. *Nature Methods* 2019, 16 (2), 171–174. [PubMed: 30664778]
80. Marvin JS; Borghuis BG; Tian L; Cichon J; Harnett MT; Akerboom J; Gordus A; Renninger SL; Chen T-W; Bargmann CI; Orger MB; Schreiter ER; Demb JB; Gan W-B; Hires SA; Looger LL, An optimized fluorescent probe for visualizing glutamate neurotransmission. *Nature Methods* 2013, 10, 162. [PubMed: 23314171]
81. Patriarchi T; Cho JR; Merten K; Howe MW; Marley A; Xiong W-H; Folk RW; Broussard GJ; Liang R; Jang MJ; Zhong H; Dombeck D; von Zastrow M; Nimmerjahn A; Gradinaru V; Williams JT; Tian L, Ultrafast neuronal imaging of dopamine dynamics with designed genetically encoded sensors. *Science* 2018, 360 (6396), eaat4422. [PubMed: 29853555]

82. Hendel T; Mank M; Schnell B; Griesbeck O; Borst A; Reiff DF, Fluorescence Changes of Genetic Calcium Indicators and OGB-1 Correlated with Neural Activity and Calcium In Vivo and In Vitro. *The Journal of Neuroscience* 2008, 28 (29), 7399–7411. [PubMed: 18632944]
83. Lock JT; Parker I; Smith IF, A comparison of fluorescent Ca²⁺ indicators for imaging local Ca²⁺ signals in cultured cells. *Cell Calcium* 2015, 58 (6), 638–648. [PubMed: 26572560]
84. Tang S; Reddish F; Zhuo Y; Yang JJ, Fast kinetics of calcium signaling and sensor design. *Current Opinion in Chemical Biology* 2015, 27, 90–97. [PubMed: 26151819]
85. Lapray D; Laszotci B; Lagler M; Viney TJ; Katona L; Valenti O; Hartwich K; Borhegyi Z; Somogyi P; Klausberger T, Behavior-dependent specialization of identified hippocampal interneurons. *Nature Neuroscience* 2012, 15, 1265. [PubMed: 22864613]
86. Llinás R; Sugimori M, Electrophysiological properties of in vitro Purkinje cell somata in mammalian cerebellar slices. *The Journal of Physiology* 1980, 305 (1), 171–195. [PubMed: 7441552]
87. Tochitsky I; Polosukhina A; Degtyar Vadim E.; Gallerani N; Smith Caleb M.; Friedman A; Van Gelder Russell N.; Trauner D; Kaufer D; Kramer Richard H., Restoring Visual Function to Blind Mice with a Photoswitch that Exploits Electrophysiological Remodeling of Retinal Ganglion Cells. *Neuron* 2014, 81 (4), 800–813. [PubMed: 24559673]
88. Euler T; Hausselt SE; Margolis DJ; Breuninger T; Castell X; Detwiler PB; Denk W, Eyecup scope—optical recordings of light stimulus-evoked fluorescence signals in the retina. *Pflügers Archiv - European Journal of Physiology* 2009, 457 (6), 1393–1414. [PubMed: 19023590]
89. Farber DB; Flannery JG; Bowes-Rickman C, The rd mouse story: Seventy years of research on an animal model of inherited retinal degeneration. *Progress in Retinal and Eye Research* 1994, 13 (1), 31–64.
90. Bowes C; Li T; Danciger M; Baxter LC; Applebury ML; Farber DB, Retinal degeneration in the rd mouse is caused by a defect in the β subunit of rod cGMP-phosphodiesterase. *Nature* 1990, 347 (6294), 677–680. [PubMed: 1977087]
91. Telias M; Denlinger B; Helft Z; Thornton C; Beckwith-Cohen B; Kramer RH, Retinoic Acid Induces Hyperactivity, and Blocking Its Receptor Unmasks Light Responses and Augments Vision in Retinal Degeneration. *Neuron* 2019, 102 (3), 574–586.e5. [PubMed: 30876849]
92. Stasheff SF, Emergence of Sustained Spontaneous Hyperactivity and Temporary Preservation of off Responses in Ganglion Cells of the Retinal Degeneration (rd1) Mouse. *Journal of Neurophysiology* 2008, 99 (3), 1408–1421. [PubMed: 18216234]
93. Menzler J; Zeck G, Network Oscillations in Rod-Degenerated Mouse Retinas. *The Journal of Neuroscience* 2011, 31 (6), 2280–2291. [PubMed: 21307264]
94. Butkevich AN; Bossi ML; Lukinavius G; Hell SW, Triarylmethane Fluorophores Resistant to Oxidative Photobleaching. *Journal of the American Chemical Society* 2019, 141 (2), 981–989. [PubMed: 30562459]
95. Deal PE; Liu P; Al-Abdullatif SH; Muller VR; Shamardani K; Adesnik H; Miller EW, Covalently Tethered Rhodamine Voltage Reporters for High Speed Functional Imaging in Brain Tissue. *Journal of the American Chemical Society* 2020, 142 (1), 614–622. [PubMed: 31829585]
96. Grenier V; Daws BR; Liu P; Miller EW, Spying on Neuronal Membrane Potential with Genetically Targetable Voltage Indicators. *Journal of the American Chemical Society* 2019, 141 (3), 1349–1358. [PubMed: 30628785]
97. Alivisatos AP; Chun M; Church George M.; Greenspan Ralph J.; Roukes Michael L.; Yuste R, The Brain Activity Map Project and the Challenge of Functional Connectomics. *Neuron* 2012, 74 (6), 970–974. [PubMed: 22726828]
98. Hillman EMC; Voleti V; Patel K; Li W; Yu H; Perez-Campos C; Benezra SE; Bruno RM; Galwaduge PT, High-speed 3D imaging of cellular activity in the brain using axially-extended beams and light sheets. *Current Opinion in Neurobiology* 2018, 50, 190–200. [PubMed: 29642044]
99. Wu J; Liang Y; Chen S; Hsu C-L; Chavarha M; Evans SW; Shi D; Lin MZ; Tsia KK; Ji N, Kilohertz two-photon fluorescence microscopy imaging of neural activity in vivo. *Nature Methods* 2020, 17 (3), 287–290. [PubMed: 32123392]

100. Tanese D; Weng J-Y; Zampini V; de-Sars V; Canepari M; Rozsa B; Emiliani V; Zecevic D, Imaging membrane potential changes from dendritic spines using computer-generated holography. *Neurophotonics* 2017, 4 (3), 031211. [PubMed: 28523281]
101. Pégard NC; Mardinly AR; Oldenburg IA; Sridharan S; Waller L; Adesnik H, Three-dimensional scanless holographic optogenetics with temporal focusing (3D-SHOT). *Nature Communications* 2017, 8 (1), 1228.
102. Kazemipour A; Novak O; Flickinger D; Marvin JS; Abdelfattah AS; King J; Borden PM; Kim JJ; Al-Abdullatif SH; Deal PE; Miller EW; Schreiter ER; Druckmann S; Svoboda K; Looger LL; Podgorski K, Kiloherz frame-rate two-photon tomography. *Nature Methods* 2019, 16 (8), 778–786. [PubMed: 31363222]

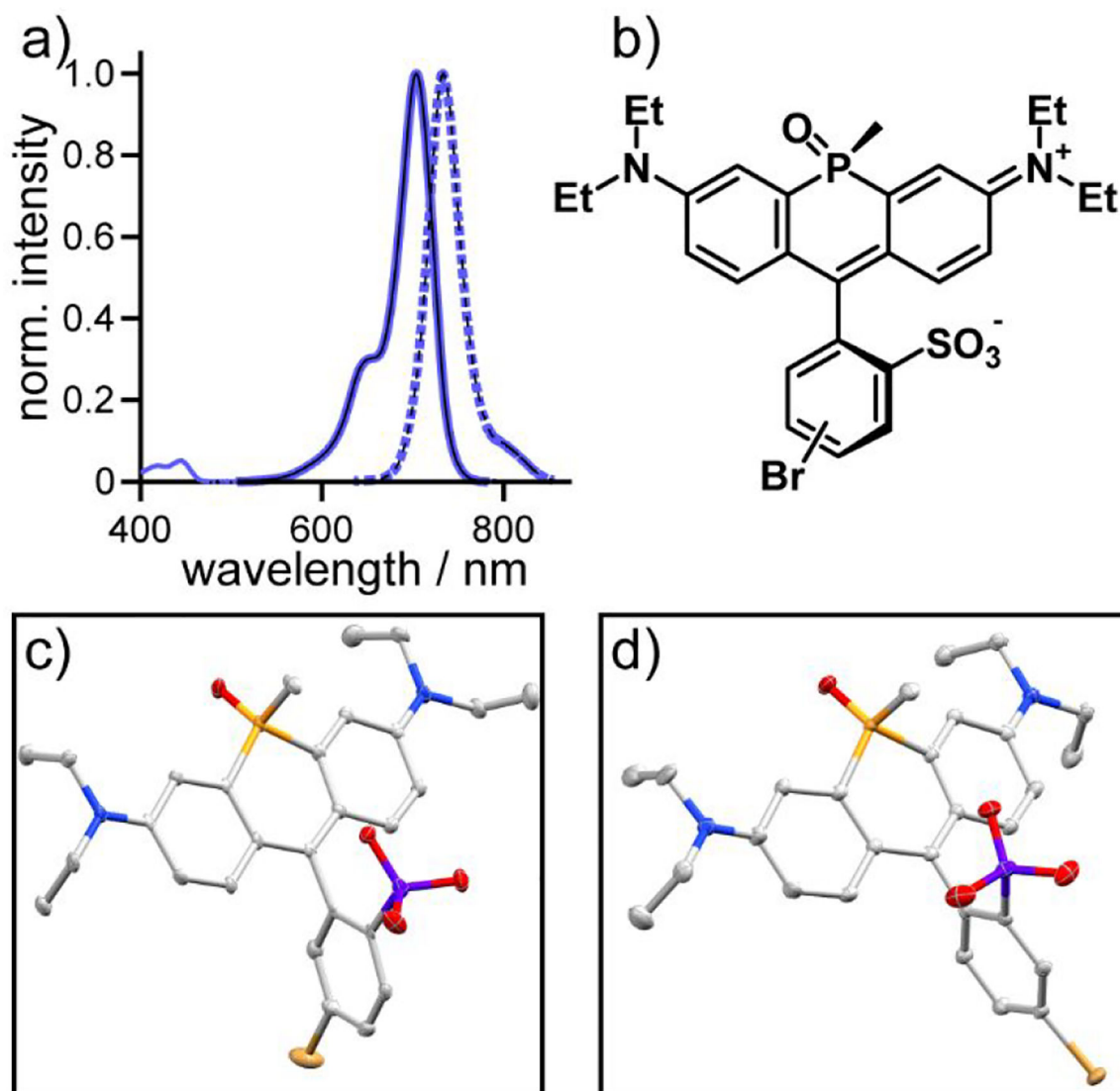


Figure 1. Characterization of sulfonated phosphine-oxide rhodamine dyes **8** and **9**. **a)** Plots of normalized absorbance (solid lines) and fluorescence intensity (dashed lines; excitation provided at 625 nm) of phosphine-oxide rhodamine **8** (thick blue lines) and **9** (black lines) in phosphate buffered saline (5 μ M dye, 1% DMSO). **b)** Chemical structure of the *cis* isomers of **8** and **9**. Thermal ellipsoid plots (50%) of **c)** **8** and **d)** **9**. Hydrogen atoms, lattice solvent molecules and resolved disordered fragments have been omitted for clarity.

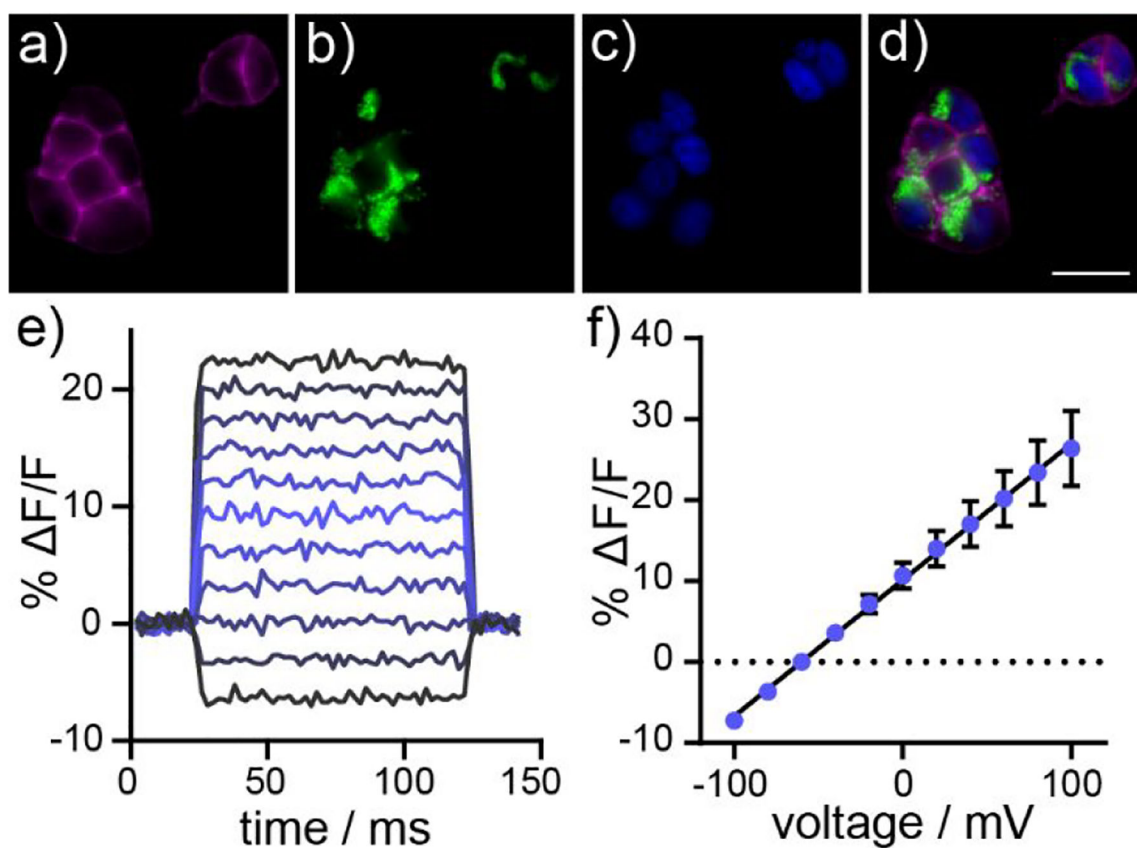


Figure 2. Cellular characterization of poRhoVR indicators in HEK cells. (a-d) Widefield, epifluorescence images of a) poRhoVR **14** (1 μ M) in HEK cells. Cells are counter-stained with b) rhodamine 123 (1 μ M) and c) Hoechst 33342 (1 μ M) to visualize mitochondria and nuclei, respective. d) An overlay of poRhoVR **14**, rhodamine 123, and Hoechst 33342. Scale bar for (a-d) is 20 μ m. e) Plot of fractional change in fluorescence of poRhoVR **14** vs time for 40 ms hyper- and depolarizing voltage steps from a holding potential of -60 mV for a single HEK cell labeled with poRhoVR **14** (1 μ M). f) Plot of $\Delta F/F$ vs membrane potential, summarizing data from $n = 6$ individual HEK cells. Error bars are \pm S.D. If error bars are not visible, the error is smaller than the marker.

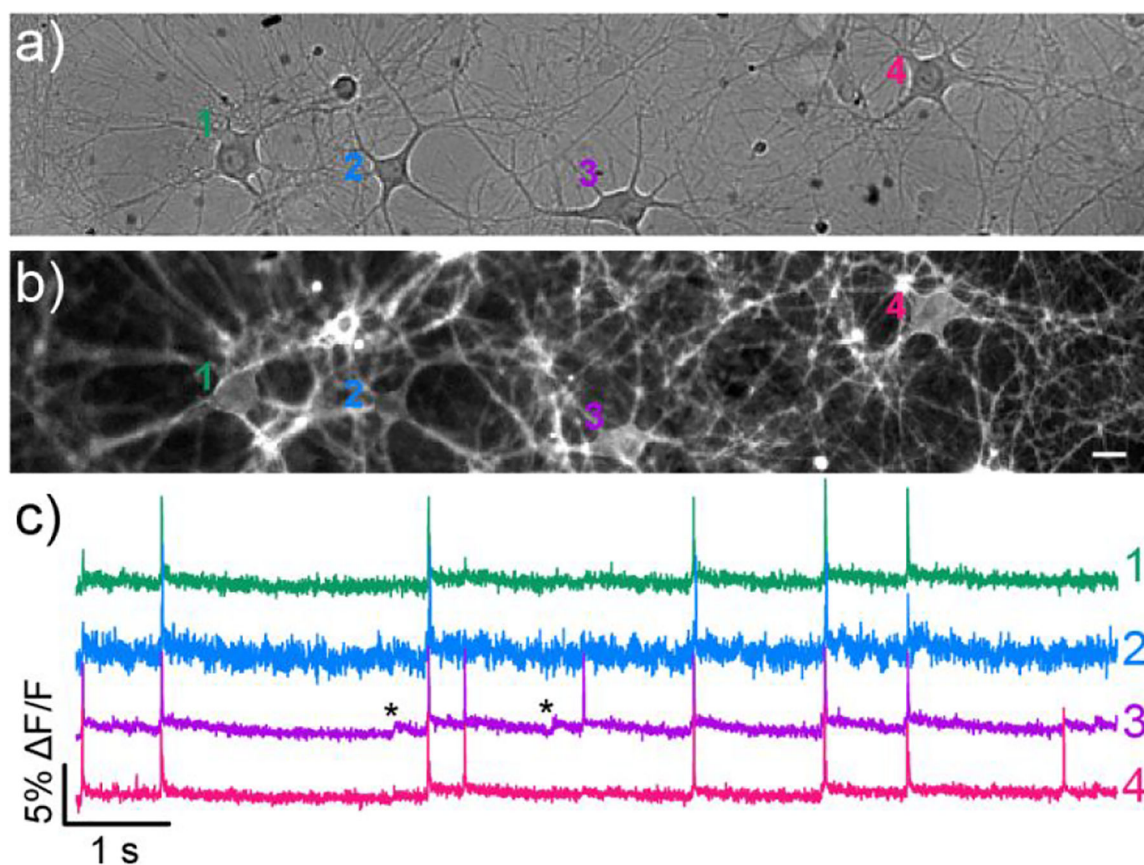


Figure 3.

Voltage imaging in dissociated rat hippocampal neurons with poRhoVR **14**. Transmitted light image of neurons loaded with **a**) poRhoVR **14** (500 nM). **b**) Epifluorescence image of neurons showing poRhoVR **14** staining. Scale bars are 20 μm . **c**) Plot of fractional change in poRhoVR **14** fluorescence ($\Delta F/F$) vs time emanating from cells 1–4 in image (**b**). Optical sampling rate is 500 Hz. Asterisks indicate subthreshold voltage changes.

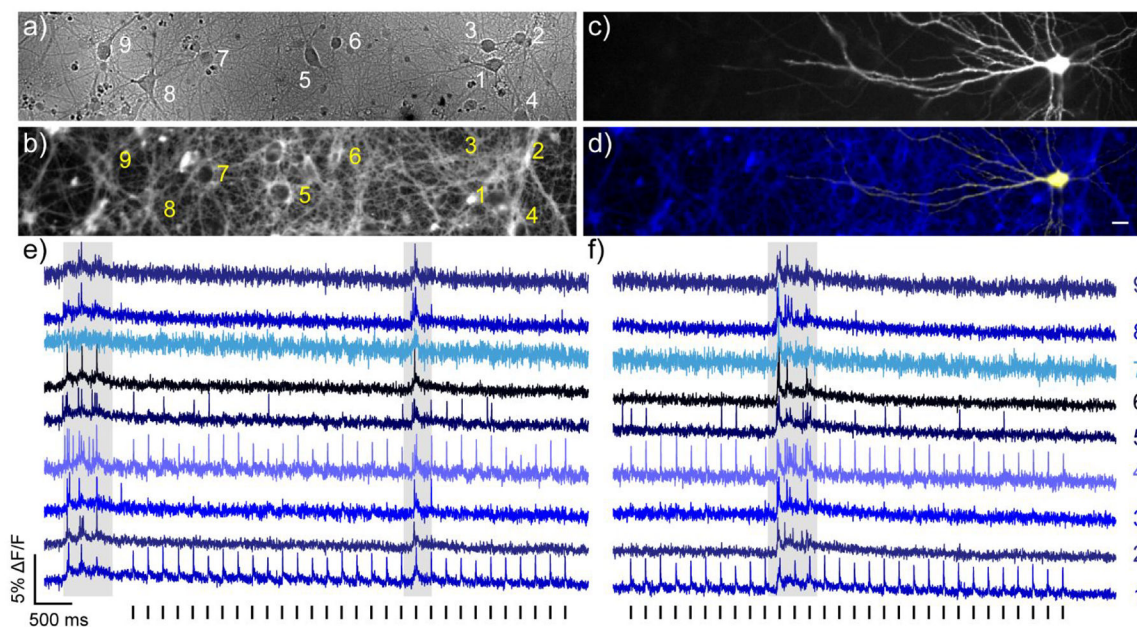


Figure 4.

All-optical electrophysiology using poRhoVR **14** and ChR2. **a)** Transmitted light image of dissociated rat hippocampal neurons stained with poRhoVR **14** (500 nM). Scale bar is 20 μm . **b)** Epifluorescence image of neurons stained with poRhoVR **14**. **c)** Epifluorescence image of neuron displaying YFP marker of ChR2 expression. **d)** Composite image depicting poRhoVR **14** labeling and ChR2-YFP expression. **e)** Recording of $\Delta F/F$ from the cell bodies of neurons indicated in panels **a-d**. **f)** Plot of $\Delta F/F$ from the cell bodies of neurons indicated in panels **a-d**, recorded 90 seconds after the data shown in panel **e**. Optical sampling rate was 500 Hz. The entire field was stimulated optically with flashes of cyan light (475 nm, 5 ms, 1.92 mW/mm^2) as indicated by the vertical bars below the blue optical recording in panels **e** and **f**. Optical voltage recordings are single trials.

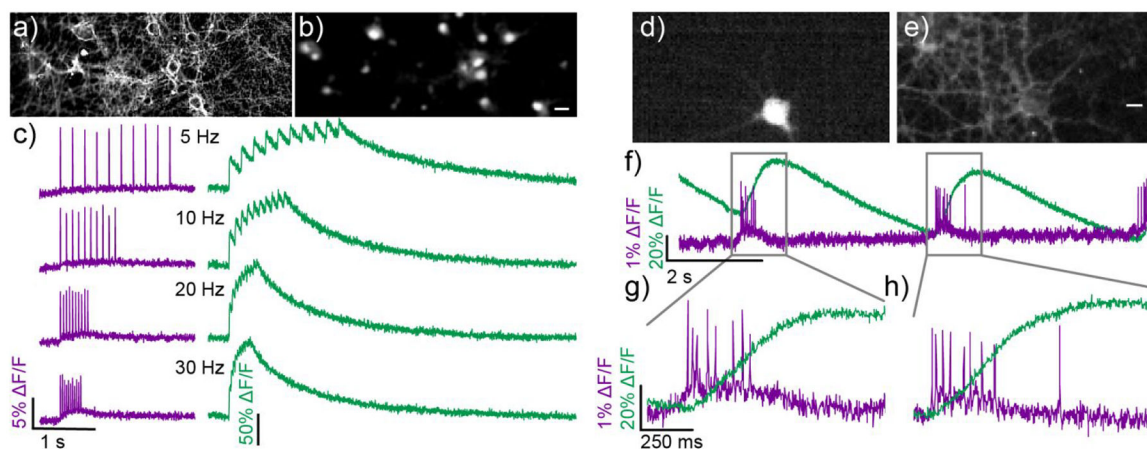


Figure 5.

Simultaneous voltage and calcium imaging with poRhoVR **14**. Epifluorescence image of neurons stained with both **a)** poRhoVR **14** (1 μ M) and **b)** Oregon Green BAPTA 1 AM (OGB, 1 μ M). **c)** Plots of $\Delta F/F$ for voltage (poRhoVR **14**, purple) and Ca^{2+} transients (OGB, green) in response to field stimulation driven at 5, 10, 20, and 30 Hz. **d)** Epifluorescence image of a neuron transfected with GCaMP6s. **e)** This same GCaMP6s (+) neuron is also stained with poRhoVR **14** and imaged simultaneously. Scale bar is 10 μ m. **f)** Simultaneously recorded traces of voltage and calcium activity from neuron in panels **d)** and **e)**. Activity was evoked using field stimulation at a rate of 16 Hz. **g)** The insets show that the onset and decay of voltage signals imaged with poRhoVR **14** precede that of the calcium signal visualized from the same cell with GCaMP6s.

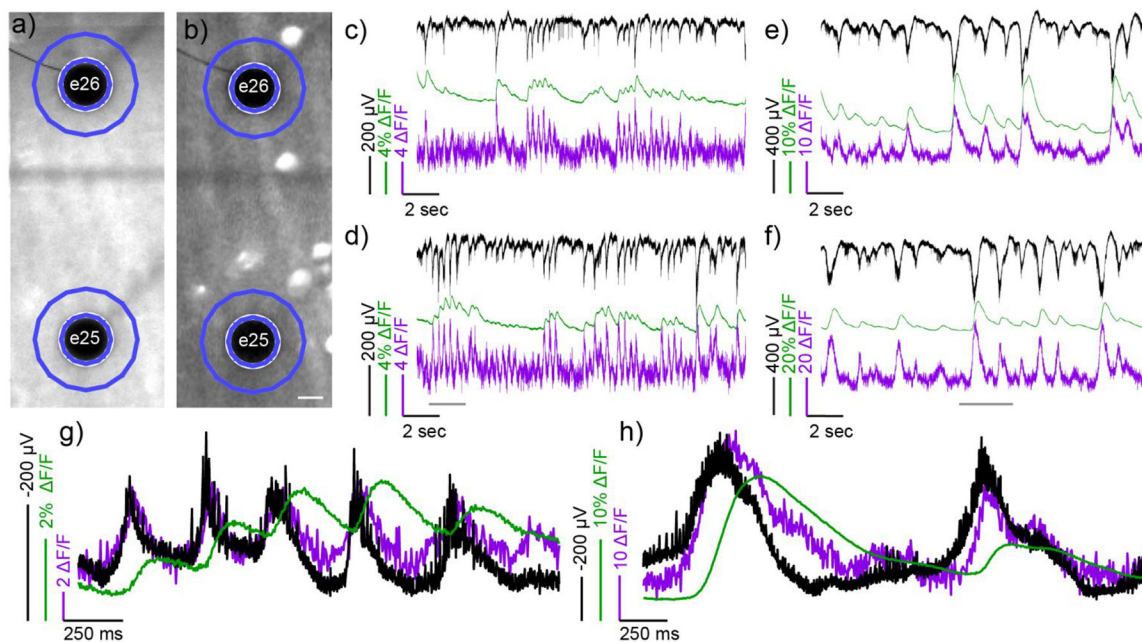
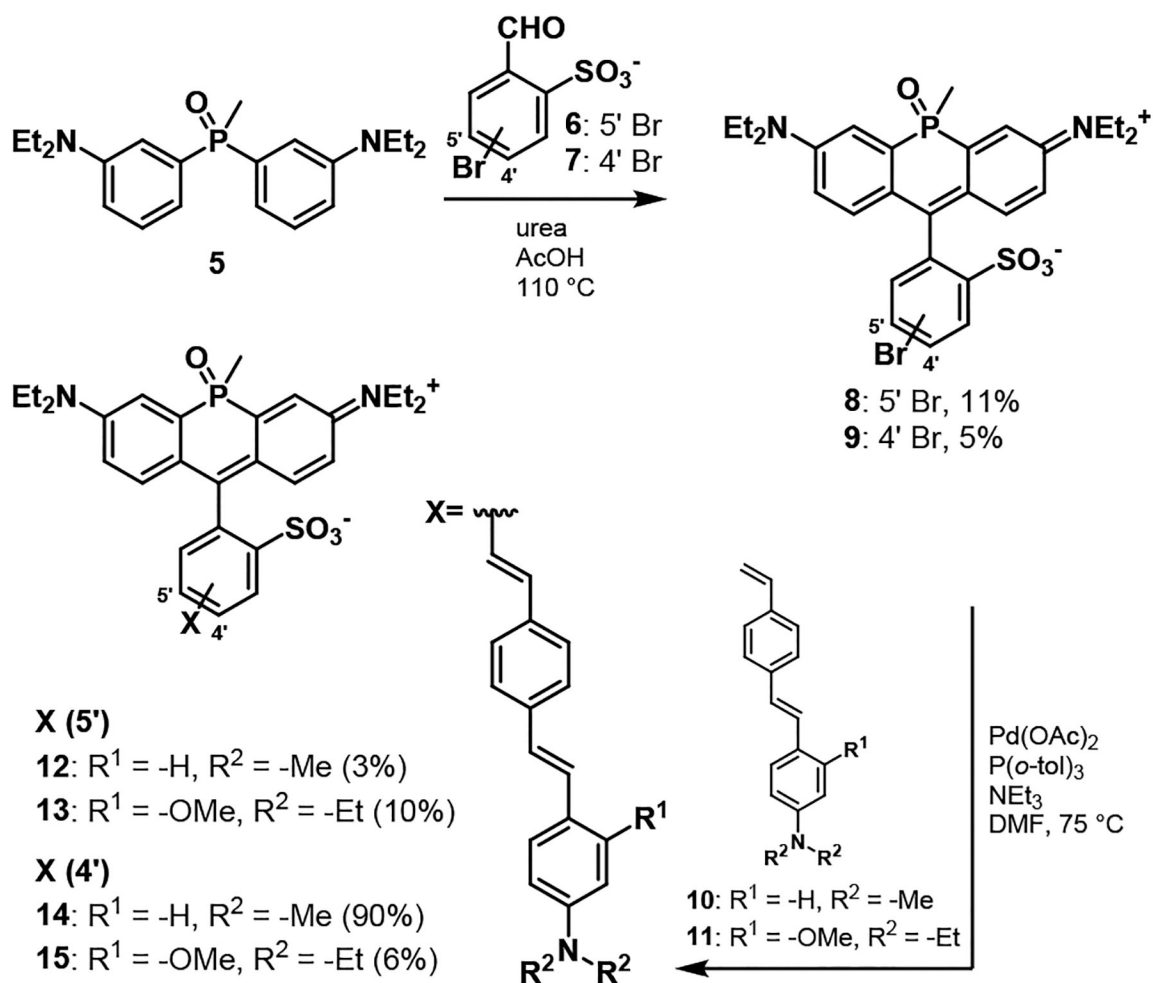


Figure 6.

Simultaneous mapping of electrical and Ca^{2+} activity using poRhoVR, GCaMP6f and multi-electrode arrays (MEA) in *ex vivo* retinas from *rd1* mice. Widefield fluorescence micrographs of retina stained with **a**) poRhoVR **14**; the retinal ganglion cells (RGCs) express **b**) GCaMP6f. The black dots are MEA electrodes, labeled numerically, underneath the retina. Scale bar is 20 μm . Recordings **c-f** depict MEA, GCaMP6f, and poRhoVR **14** signals vs. time. Traces are as follows: raw MEA electrical signal (black), bleach corrected poRhoVR F/F (arbitrary units) (magenta), and GCaMP6f F/F (%) (green). Optical signals are from the regions of interest (ROIs) indicated in blue in panels **a** and **b**. Panels **c** and **d** depict the spontaneous activity in the retina prior to addition of synaptic blockers. Panels **e** and **f** show MEA, GCaMP6f, and poRhoVR **14** signals 15 min. after the addition of synaptic blockers. Panels **c** and **e** correspond to signals associated with electrode 26 (e26), and panels **d** and **f** correspond to signals associated with electrode 25 (e25). Panels **g** and **h** show zoomed-in regions of e25, from the time period indicated by a grey bar in panel **d** and **f**, respectively. In panels **g** and **h**, the MEA signal (black) is inverted to facilitate comparison with optical voltage recordings with poRhoVR (magenta).

**Scheme 1.**

Synthesis of sulfonated phosphine oxide rhodamine voltage reporters (poRhoVRs)

Properties of po-RhoVR indicators

Table 1.

Compound number	isomer ^a	R ¹	R ²	$\lambda_{\text{abs}} / \text{nm}$ ^b	$\lambda_{\text{em}} / \text{nm}$ ^b	Φ ^b	rel. cell brightness ^c	F/F ^d
8	<i>meta</i>	n/a	n/a	704	728	0.22	n/a	n/a
9	<i>para</i>	n/a	n/a	704	728	0.19	n/a	n/a
12	<i>meta</i>	H	Me	705	731	0.01	1.5 ± 0.9	13 ± 0.3%
13	<i>meta</i>	OMe	Et	703	728	0.01	1.0 ± 0.1	43 ± 0.9%
14	<i>para</i>	H	Me	704	723	0.07	12 ± 0.1	17 ± 0.5%
15	<i>para</i>	OMe	Et	704	726	0.09	1.3 ± 0.03	31 ± 0.5%

^a Relationship between fluorophore and molecular wire^b dPBS with 0.1% DMSO^c Relative cellular brightness, in HEK cells^d per 100 mV, in HEK cells. Data are mean ± S.E.M. for at least 3 separate determinations.